EFFECT OF Cr AND Ni CONTENTS ON THE OXIDATION BEHAVIOR OF FERRITIC AND AUSTENITIC MODEL ALLOYS IN AIR WITH WATER VAPOR.

R. Peraldi and B. A. Pint

Metals and Ceramics Division
Oak Ridge National Laboratory
Oak Ridge, TN 37831-6156

KEYWORDS

Ferritic stainless steels, Austenitic stainless steels, Fe-Cr, Fe-Cr-Ni, Water Vapor, Breakaway Oxidation, Accelerated attack, Spallation.

ABSTRACT

Ferritic and austenitic model alloys with various contents of Cr and Ni ranging between 10-20% and 0-30% respectively, were oxidized in air + 10% water vapor during 1h cyclic oxidation at 650 and 800°C. Depending on the alloy composition and temperature, either a thin protective oxide scale was observed or accelerated attack occurred which sometimes included spallation. For austenitic model alloys, increasing either the Cr or Ni contents delayed the accelerated attack. For lower Cr and Ni contents at 800°C, accelerated attack, including spallation, occurred at short exposure times. No spallation was observed for the ferritic model alloys. However, accelerated attack can occur quickly with low Cr contents. Increasing the temperature delayed the breakaway observed on ferritic alloys whereas it reduced the protective oxide growth stage for austenitic alloys.

INTRODUCTION

The oxidation performance of stainless steels used in high-temperature applications (such as heat exchangers in power generation) depends on their potential to form and maintain a Cr-rich protective oxide scale. Most stainless steels are well known for their ability to form and maintain a Cr_2O_3 oxide scale under dry atmospheres. However, this behavior must be reevaluated when water vapor is present in the oxidizing atmosphere [1]. The presence of water vapor (wet air, wet oxygen or steam) can have a dramatic effect on stainless steel oxidation behavior, inducing a rapid and catastrophic oxidation (accelerated attack or breakaway) where a non-protective iron-rich oxide scale forms and reduces the expected performance life of the alloy. Higher water vapor partial pressures or faster gas flow rates reduced the protective behavior of scales [2-3], and one alternative appeared to be selecting alloys with higher Cr contents (above 20-25%) [4-5]. However, this strategy greatly increases the alloy cost and may be detrimental to the mechanical properties.

Numerous factors play a role in water vapor effects. An important one is the diffusivity of Cr in the alloy, with differences expected between ferritic and austenitic alloys, or alloys with different grain size, or with different amounts of surface deformation to alter the density of fast diffusion paths (grain boundaries and dislocations) [6-7]. This study was undertaken to provide a clear, fundamental understanding of the role of alloy composition and phase content on the corrosion resistance of stainless steels in wet atmospheres. The oxidation behavior of several ferritic and austenitic model alloys was examined under mixed air+10% water vapor to simulate exhaust gas environments. These model alloys (free of minor alloying elements) cover a large range of Ni and Cr contents: between 0-30wt.% and 10-20wt.%, respectively. The goal of the first part of this study was to determine the critical Cr content and the effect of Ni concentration in order to avoid the accelerated corrosion attack caused by water vapor. Later stages will examine the effect of alloy grain size and minor alloying

elements (e.g. Mn, Si) in order to develop guidelines for low-cost stainless steels that are resistant to water vapor attack.

EXPERIMENTAL PROCEDURE

The model alloys were vacuum induction melted and solidified in water-cooled copper molds. Chemical compositions of the as-cast alloys are listed in Table 1. These inductively coupled plasma (ICP) quantitative analyses show that the actual compositions of the alloys were close to the nominal levels. The amounts of metallic and metalloid impurities were less than 0.04 and 0.2wt% respectively. Prior to cutting into oxidation coupons, all of the alloys were vacuum annealed for 4 hours at 1100°C in sealed quartz ampoules. Disc-shaped specimens (1mm thick, ≈15mm diameter) were cut from each casting and polished to 600-grit SiC paper. Prior to oxidation, samples were cleaned in acetone and methanol. In Figure 1, optical micrographs of the annealed and etched alloys are shown with corresponding X-ray diffraction results. Model alloys without Ni are fully ferritic, whereas those with Ni contents higher than 10% are all austenitic. Average grain sizes (about 150-300μm) of these specimens were similar. Only the Fe-XCr-10Ni model alloys, which were both austenitic and ferritic, showed a smaller grain size.

The oxidation exposures reported here were in air with injected water (10vol.% water vapor) at 650 and 800°C. Distilled water was atomized into the flowing gas stream above its condensation temperature and heated to the reaction temperature within the furnace alumina tube. Cycle times at temperature were 1h with 10min cooling between cycles. Samples were hung from an alumina rod and attached by Pt-Rh wire. Mass change data were generated by weighing the specimens every 20h using a Mettler model AG245 balance.

The surfaces of the exposed specimens were examined using light microscopy (LM) and secondary electron microscopy (SEM) in order to characterize the surface morphology of the oxide

scales. X-Ray diffraction (XRD) analyses using Cu-K_α radiation were made on these surfaces to determine the oxide phases. Then, selected specimens were Cu-plated and sectioned for metallographic examination using LM, SEM, back-scattered electron microscopy (BSEM), energy dispersion X-ray analysis (EDX) and/or electron probe microanalysis (EPMA) for characterization of the oxide scale.

EXPERIMENTAL RESULTS

Specimen mass change

Figure 2 shows the effects of Cr and Ni contents on the specimen mass change of Fe-Cr-Ni alloys during oxidation at 650°C. Depending on the alloy composition and on the oxidation temperature, three different behaviors were observed: i) growth of a thin protective oxide scale (POS) with a corresponding small mass change, ii) accelerated attack without spallation (AA) which is noted by a large positive mass change corresponding to the fast growth of an unprotective oxide scale, iii) accelerated attack with oxide spallation (AAS) which is characterized by a large mass loss. For alloys with 16%Cr, AAS was observed for Fe-16Cr-10Ni after 20x1h cycles, whereas 80x1h cycles of oxidation were needed for Fe-16Cr-15Ni. AA was observed for Fe-16Cr-20Ni for 80x1h cycles whereas the growth of a POS was observed up to 100 cycles for higher Ni contents (≥25%). The same conclusion can generally be made for Fe-18Cr-Ni (Figure 2b) and Fe-20Cr-Ni (Figure 2c, with an expanded Y-axis). Comparing the behavior of these model alloys with the same Ni content, the beneficial effect of a higher Cr concentration is clear. For alloys with 20%Cr, the growth of a POS was observed for all Ni contents. Figure 2c also shows that a small mass loss was observed during the growth of the POS. At 800°C (Figure 3), the behavior of Fe-Cr-Ni steels was similar: both higher Cr and Ni contents delayed the AA or AAS. However, at this higher temperature, a POS could not be maintained for 100h for any of the compositions. It should be noted that the specimen mass gains or

mass losses were higher at 800°C than at 650°C. Therefore, for these Fe-Cr-Ni model alloys, increasing the oxidation temperature led to faster breakaway with more spallation of the scale and/or a thicker non-protective scale.

For the Fe-Cr ferritic alloys, no scale spallation was observed for any of the specimens (Figure 4). At 650°C, all of the specimens showed AA. Specimens with 18 and 20%Cr showed protective behavior after 20x1h but then showed AA (Figure 4a). The final mass gain after 100h decreased with increasing Cr content. At 800°C, AA was observed for lower Cr content (≤14%) specimens whereas a POS was observed after 100x1h cycles for higher Cr contents (≥16), Figure 4b. A small mass loss was observed for these specimens after 20 cycles, likely due to Cr_2O_3 evaporation (Figure 4c). Thus, for ferritic Fe-Cr alloys, increasing both temperature and Cr content enhanced the growth of a POS.

Characterization of the oxide scales

Figure 5 shows LM of the samples after 100x1h cycles at 650°C for representative Fe-Cr-Ni alloys. Both XRD and SEM results also are included in Figure 5. The morphology of the POS appeared uniform across the specimen (Figures 5c-d). A SEM micrograph of the scale shows facetted Cr_2O_3 oxide grains, Figure 5d. For lower Ni and Cr contents, the growth of a reddish Fe_2O_3 oxide scale was observed near the edge and the hole of the sample (Figure 5b) and likely corresponded to the first step of an AA characterized by the growth of oxide whiskers. As the mass gain corresponding to the growth of these whiskers might be small, this first step of the AA would not be observed in the specimen mass change (e.g., Fe-20Cr-10Ni in Figure 2c). For lower Cr and Ni contents, following the growth of oxide whiskers, spallation of a part of the oxide scale occurred (e.g. Figure 5a). This resulted in a cellular morphology. On these cells, the growth of oxide blades or platelets was observed and these regions corresponded to reddish areas of the sample surface whereas the darker areas were associated with a non-uniform rough and spalled oxide morphology (Figure 5a). Both Fe_2O_3 and Fe_3O_4

were detected by XRD on this sample. At 800°C, the main morphology of the AAS samples was characterized by a cellular morphology that was rough and cracked due to macroscopic deformation of the specimen (Figures 6a-c). Morphology of AA scales (Fe_2O_3 + Fe_3O_4) showed open pores and the nucleation of some small grains (Figures 6d).

For the Fe-Cr model alloys, the reaction products were relatively uniform, Figures 7a-f. The surface morphology was either characterized by the growth of whiskers on an oriented cellular scale (Fe_2O_3) when AA occurred (Figure 7e), or by small Cr_2O_3 grains of the POS (Figure 7f). At 650°C, one other XRD peak (2Θ=61.09°) was observed but could not be clearly identified (Figures 7a and c).

LM of cross sections of Fe-Cr-Ni alloys oxidized at 650 and 800°C are shown with compositions labeled from EDX and EPMA analyses, Figures 8 and 9, respectively. The very thin POS were Cr-rich corundum $(Cr,Fe)_2O_3$ phase (Figures 8c-e). As these oxide scales were very thin and rough, accurate quantitative determination of the Fe content was difficult. A small Cr depletion in the alloy, a few microns below the oxide scale, was found on Fe-20Cr-30Ni (Figure 8e). The minimum Cr content detected was 18.3±0.2at% (17.2±0.2wt%) reduced from the starting content of 21.1±0.2at.% (19.7±0.2wt%). No Ni depletion was observed. Both POS and AA scales formed at 650°C were observed on Fe-20Cr-10Ni (Figures 8b-c). This first step of AA was characterized by the growth of iron-rich nodules. The thicker AA scales were more uniform and consisted of 3 different layers (Figures 8a and 9). The Fe_2O_3 external layer contained 0.2-0.3at% of Cr and 0.1-0.2at% of Ni . The intermediate layer contained 40-50at% of Fe, 30-40at% of Cr and 20at% of Ni, and was associated with a spinel $(Fe,Cr,Ni)_XO_1$ phase with X ranging between 0.8 and 1.0. This layer is likely a mixture of iron rich-(Fe,Cr,Ni)O and iron rich-$(Fe,Cr,Ni)_3O_4$. The inner layer with about the same proportions of Fe, Cr and Ni was more difficult to analyze as a stoichiometric oxide as X ranged between 1.4 and 1.7 (Figures 8a and 9b). No Cr depletion was found in the alloy below these thick oxide scales. The compositions of both AA and AAS oxide scales obtained at 650 and 800°C were similar.

For Fe-Cr model alloys, the Cr-rich $(Cr,Fe)_2O_3$ scale grew on a Cr-depleted alloy (Figures 10d and f). The Cr content on Fe-20Cr alloy near the oxide/metal interface was about 17.4±0.2at.% (16.4±0.2wt%) whereas the nominal content of the alloy (20.6±0.2at.% or 19.5±0.2wt%) was found about 15µm from the oxide/alloy interface (Figure 10f). The AA scales (Figures 10a-c and e) were thicker and showed less interfacial roughness and fewer defects (pores and cracks) than AA scales formed on Fe-Cr-Ni alloys, but also contained 3 layers. In all cases, the external layer was analyzed as Fe_2O_3 with less than 0.1±0.2at.% Cr. The Fe_3O_4 intermediate layer contained 0-0.4at.% Cr. At 650°C, the inner layer was Fe-rich $(Fe,Cr)_3O_4$ spinel with a Cr content ranging between 20 and 50at.%. The Cr content in the oxide increased with increasing Cr in the alloy. At 800°C, $(Fe_{0.75},Cr_{0.25})_{0.85}O_1$ was identified on Fe-10Cr model alloys.

The AA formed at 800°C contained more microstructural defects (cracks, pores) than at 650°C (Figures 10a-b). The defects were both perpendicular (especially those found in the outer part of the oxide scale), and parallel to the oxide/alloy interface (Figure 10b). Large cracks due to macroscopic deformation at 800°C (Figures 6a-c) could also be observed on cross-sections of the austenitic alloys (black block arrows in Figures 9b-c). Less macroscopic deformation was observed for the ferritic alloys. In general, the crystallographic orientation of the alloy grains (white block arrows in Figure 10a), as well as the presence of grain boundaries (white block arrows in Figures 9b-c), seemed to influence scale growth (especially for the inner layer) and defect density in the oxide.

DISCUSSION

Mass change-microstructure correlation

Microstructures of the oxide scales obtained on both Fe-Cr-Ni and Fe-Cr model alloys corresponding to POS, AA or AAS can be correlated to the specimen mass changes:

i) POS: For very small mass gain, the growth of the very thin protective Cr-rich $(Cr,Fe)_2O_3$ scale was observed. The morphology of the POS characterized by fine grains typical of a Cr-rich $(Cr,Fe)_2O_3$ scale was in good agreement with those previously reported in the literature [8-10]. During the growth of a POS, a small specimen mass loss was observed on both austenitic and ferritic alloys (Figures 2c and 4c) which was likely the result of volatilization of some Cr species. It has been speculated that water vapor accelerates the formation of volatile species such as CrO_3, $CrO_2(OH)$ or especially $CrO_2(OH)_2$ [11] which changes the $(Fe,Cr)_2O_3$ scale from a Cr-rich POS to a non-protective α-Fe_2O_3 scale [7]. Therefore, increasing the water vapor partial pressure and/or the gas velocity would be expected to result in less protective behavior of stainless steels [12]. Another study calculated that the Cr_2O_3 volatilization rate could be negligible during oxidation of stabilized ferritic steels under Ar+15%H_2O suggesting that evaporation may not be the only important mechanism [3].

ii) Transition from POS to AA: The first stage of the AA scales formed on Fe-Ni-Cr and Fe-Cr alloys showed a porous-cellular morphology with whiskers [13-14]. This very first step of the AA might correspond to a slight increase of the specimen mass change. However, competition with mass loss due to vaporization (or spallation) could make it difficult to detect. In many cases, the first sign of the AA usually occurred near the edges of the samples (e.g. Figure 5b). For these 1h cyclic exposures, it is likely that the high cycle frequency with the associated thermal stresses could cause scale spallation near the specimen edge leading to AA. Also, the AA could be enhanced near the edge where, because of the higher surface/volume, the Cr content could become depleted more quickly than near the center of the specimen.

iii) Thick AA and AAS: When the entire surface of the oxidized sample showed AA, the specimen mass change increased and could be easily detected. The whiskers observed on the surface of the sample are indicative of α-Fe_2O_3 and support the XRD and EPM results that the underlying oxide layer also is α-Fe_2O_3. The microstructure of the AA or AAS scales grown on Fe-Cr-Ni alloys were

characterized by three different oxide layers: an external scale of Fe_2O_3, an intermediate layer of $(Fe,Cr,Ni)_{0.8\text{-}1}O_1$ and an inner layer of $(Fe,Cr,Ni)_{1.4\text{-}1.7}O_1$. For the Fe-Cr alloys, the three layers were: Fe_2O_3, Fe_3O_4 and $(Fe_{0.5\text{-}0.8},Cr_{0.2\text{-}0.5})_3O_4$. Such a three layer structure has been previously observed [15]. However some studies reported only two layers growth in steam: an external layer of Fe_3O_4 and an inner scale of $(Fe,Cr)_3O_4$ [5, 13]. The absence of the Fe_2O_3 layer could be due to spallation during cooling as observed by Otsuka et al. [5] or because the low oxygen partial pressure reached in steam could prevent the formation of Fe_2O_3. The outer layers in the present study contained numerous microstructural defects (as cracks and pores) on Fe-Cr-Ni alloys (black and gray block arrows in Figures 9a-c) and spallation occurred mainly through these scales. The inner layer grown on Fe-Cr-Ni alloys has been previously characterized as spinel oxide particles dispersed within a metal matrix [5] or as sub-micron metallic particles suspended in an oxide matrix [2]. The EDX and EPMA analyses from this study support some type of metal-oxide mixture as X values ranged between 1.4 and 1.7 in $(Fe,Cr,Ni)_XO$ instead of 0.6-1.0 expected for spinel.

The AAS was associated with large mass losses. It occurred on Fe-Cr-Ni model alloys only for lower Ni and Cr contents, but not for the lower-Cr ferritic alloys. The difference in spallation behavior between ferritic and austenitic alloys could be explained because of the differences in the thermal expansion coefficient (about $18.4\text{x}10^{-6}$°C^{-1} for austenitic alloys and $14.8\text{-}15.6\text{x}10^{-6}$°$C^{-1}$ for ferritic alloys in the temperature range 650-800°C, [16]). Considering only Fe-Cr-Ni alloys, Fe-Cr-10Ni alloys that were both constituted of austenitic and ferritic phases (Table 1) all showed greater spallation at 650 and 800°C (Figures 2-3). Increasing the Ni content could alter the thermal expansion coefficient. However, there is no indication in the literature of this effect and there was no change in the room temperature lattice parameter (based on XRD) with different Ni level. An alternative explanation for the large spallation observed on the specimens with low Ni contents could be the faster growth of the non-protective scale. However, such a correlation between the amount of spallation and

the thickness of the oxide scale has not been quantitatively confirmed by these observations. Measuring the total mass change (specimen + spallation) rather than only the specimen mass change would be useful. The different oxide phases observed between the ferritic and austenitic alloys also might be a factor in the different spallation behavior.

Effects of Cr and Ni contents

Perhaps the most interesting result of this study was the determination of the Cr and Ni content needed to observe protective behavior in the presence of water vapor. Results for the Fe-Cr-Ni alloys are summarized in Figure 11 showing maps of three types of behavior observed at 650 and 800°C. It should be emphasized that these results are specific to the large as-cast grain structure. A finer alloy grain size can produce different results [17]. Also, these alloys contain none of the typical elements (Mn, Nb, Si, C, etc) found in commercial stainless steels.

The beneficial effect of increasing the Cr content is a well-known fundamental of oxidation science. Evans et al. [18] recently summarized criteria for scale failure: for a Cr_2O_3-forming alloy, intrinsic chemical failure (for highest temperature above 1117°C) is expected when the activity of Cr at the scale/alloy interface falls below the thermodynamical equilibrium of the Cr/Cr_2O_3 system. Between 650 and 800°C, this critical Cr content is close to zero. However, a mechanically-induced chemical failure can occur if the base alloy surface (after cracking and/or spalling) shows too much Cr depletion to reform a protective Cr-rich oxide layer [18]. The Cr-depletion found below the POS would support this model. Increasing the Cr content in the alloy would lower the Cr depletion at the interface for a given exposure time.

The present results also indicate a beneficial effect of increasing Ni content. This relationship has been suspected but not widely studied. Increasing the Ni content on Fe-Cr-Ni model alloys delayed the AA and/or AAS and lowered the amount of spallation. However, the role of Ni in delaying AA is not certain. Several possibilities are discussed.

i) Ni could have an effect on the Cr diffusivity in the alloy. As the oxide grain size was similar for all the alloys, enhanced Cr diffusivity could affect performance in these tests. However, no clear indication of the beneficial effect of the Ni on Cr diffusivity in stainless steels has been reported. Moreover recent measurements [19] of the coefficient of Cr diffusion in austenitic alloys showed that the diffusivity of Cr in Fe-18Cr-8Ni was slightly higher than in Fe-20Cr-32Ni (Figure 12).

ii) Ni could reduce the evaporation of the Cr-rich $(Cr,Fe)_2O_3$. However, specimen mass changes during growth of the POS were similar for all Ni contents (Figure 2c). Thus, this explanation is unlikely.

iii) Ni in the alloy is likely to become incorporated into the scale. A small amount of substituted Ni in the Cr-rich $(Cr,Fe)_2O_3$ scale could affect the defect structure and diffusivities. This explanation also appears unlikely.

iv) Ni can possibly affect the activity of Cr and/or Fe at the oxide/alloy interface. As previously reported [3, 19], catastrophic oxidation could be the result of an intrinsic effect of water vapor on the scale growth mechanism, including the inward diffusion of hydroxide ions. An effect of surface acidity on the generation of hydroxide species by decomposition of H_2O has been postulated to explain the different behavior of pure metals in water vapor [20]. It also has been shown that in mixed H_2+H_2O atmospheres, some H dissolves in the chromia scale and affects its conductivity [21-22]. Other models proposed that gaseous transport across pores with H_2O, H_2 or O_2 play an important role [13, 15]. Because of the transport of OH, H_2O or H_2 species, the activity of Cr at the alloy/oxide interface must be high enough to reform a chromia scale. The higher Ni content at this interface could increase the Cr activity and/or decrease the Fe activity, delaying the growth of iron-rich nodules corresponding to the AA.

v) Ni could lower the oxygen solubility/diffusivity in the alloy. If the mechanism by which Cr is incorporated into the inner oxide layer involves the formation of internal Cr-rich oxide precipitates in

the alloy immediately ahead of the advancing oxidation front, decreased oxygen solubility would have an effect similar to increasing the Cr activity.

Austenitic vs. Ferritic

Generally, ferritic alloys are thought to be more oxidation resistant than austenitic alloys because of their higher Cr diffusivity [7]. In the same way, a fine alloy grain size would increase the Cr diffusivity and therefore the corrosion resistance of the alloy. Comparison of Cr diffusivity in austenitic and ferritic alloys was made from diffusion data measured by Tokei et al. [19]. In Figure 12, effective diffusion coefficients (taking into account both volume diffusion and grain-boundary diffusion with an average grain size of 150μm corresponding to the alloys in this study) are shown and compared to the volume diffusion coefficient. In the temperature range of 597-805°C, the average grain size of the cast alloys was too large to strongly enhance the Cr diffusivity in both ferritic and austenitic alloys.

At 800°C, the Cr diffusivity was calculated to be more than one order of magnitude higher in the ferritic than in austenitic alloys (Figure 12) providing a plausible explanation of the better corrosion resistance of ferritic alloys. Between 600 and 650°C, the calculated Cr diffusion was similar for ferritic and austenitic alloys. Without an advantage in Cr diffusivity, the superior performance of the austenitic alloys at lower temperatures, suggests some beneficial role of Ni in improving resistance to water vapor.

SUMMARY

The oxidation behavior in water vapor-containing environments of model cast austenitic and ferritic alloys has been studied over a range of Cr (10-20wt%) and Ni (0-30wt%) contents. Increasing either the Cr or Ni content delayed the onset of accelerated attack with or without spallation. The growth of a protective Cr-rich corundum $(Fe,Cr)_2O_3$ scale was observed for higher Cr and Ni contents

at 650°C for austenitic alloys and at 800°C for Fe-Cr alloys with 16%Cr or higher. Oxide scales formed on Fe-Cr-Ni alloys after accelerated attack were characterized by three oxide layers: an external Fe_2O_3 layer, an intermediate layer of $(Fe,Cr,Ni)_{0.8\text{-}1}O_1$ and an inner layer of $(Fe,Cr,Ni)_{1.4\text{-}1.7}O_1$. For Fe-Cr model alloys, the three layers were Fe_2O_3, Fe_3O_4 and $(Fe_{0.5\text{-}0.8},Cr_{0.2\text{-}0.5})_3O_4$. For lower Ni contents, Fe-Cr-Ni showed spallation after breakaway, whereas no spallation was observed on Fe-Cr alloys. The austenitic alloys performed better at 650°C whereas the ferritic alloys performed better at 800°C. The better behavior of ferritic Fe-Cr model alloys at 800°C could be explained by a higher Cr diffusivity in the alloy. At 650°C, the better behavior of the Fe-Cr-Ni alloys suggests a beneficial effect of Ni.

ACKNOWLEDGMENTS

The authors wish to thank: G. Garner, H. Longmire, J.W. Jones and L. Walker for assistance with the experimental work. P. F. Tortorelli and I.G. Wright at ORNL reviewed this manuscript. This research is supported in part by an appointment to the Oak Ridge National Laboratory Postdoctoral Research Associates Program administered jointly by the Oak Ridge Institute For Science and Education and Oak Ridge National Laboratory, and sponsored by the Distributed Energy Resources Program, U. S. Department of Energy, under contract DE-AC05-00OR22725 with UT-Batelle, LLC.

REFERENCES

[1]: Kofstad P., “High Tempertaure Corrosion”, Elsevier Applied Science, London, 1988.

[2]: Rakowski J. M. and B. Pint, Corrosion 2000 (2000), 517 pp.1-9.

[3]: Henry S., A. Galerie and L. Antoni, Material Science Forum, Vols. 369-372 (2001), pp 353-360.

[4]: Pint B. and J. M. Rakowski, Corrosion 2000 (2000), 259 pp.1-14.

[5]: Otsuka N., Y. Shida and H. Fujikawa, Oxidation of Metals, Vol. 32, N° 1/2 (1989), pp 13-45.

[6]: Piehl C., Z. Tôkei and H.J. Grabke, Materials Science Forum, Vols. 369-372 (2001), pp 319-326.

[7]: Asteman H., Segerdahl K., J.-E. Svensson and L.-G. Johansson, Materials Science Forum, Vols. 369-372 (2001), pp 277-286.

[8]: Saeki I., H. Konno and R. Furuichi, Corrosion Science, Vol 38, N°1 (1996), pp 19-31

[9]: Saeki I., H. Konno, R. Furuichi, T. Nakamura, K. Mabuchi and M. Itoh, Corrosion Science, Vol 40, N°2/3 (1998), pp 191-200

[10]: Lobnig R.E., H.P. Schmidt, K. Hennesen and H.J. Grabke, Oxidation of Metals, Vol. 37, N° 1/2 (1992), pp 81-93.

[11]: Asteman H., Svensson J.-E., Johansson L.-G. and Norell M., Oxidation of Metals, Vol. 52, N° 1/2 (1999), pp 95-111.

[12]: Asteman H., Svensson J.-E., Norell M. and Johansson L.-G., Oxidation of Metals, Vol. 54, N° 1/2 (2000), pp 11-26.

[13]: Tomlinson L. and N.J. Cory, Corrosion Science, Vol 29, N°8 (1989), pp 939-965.

[14]: Honda K., T. Maruyama, T. Atake and Y. Saito, Oxidation of Metals, Vol 38, N°5/6 (1992), pp 347-363.

[15]: Kvernes I., M. Oliveira and P. Kofstad, Corrosion Science, Vol 17, (1977), pp 237-252.

[16]: Silberschmidt V.V. and E. Werner, Computational Materials Science, Vol 16 (1999), pp 39-52.

[17]: R. Peraldi and B.A. Pint, Oxidation of Metals, in preparation.

[18]: Evans H.E., A.T. Donaldson and T.C. Gilmour, Oxidation of Metals, Vol. 52, N° 5/6 (1999), pp 379-402.

[19]: Tökei Zs., K. Hennesen, H. Viefhaus and H. J. Grabke, Materials Science Technology, Vol 16 (2000), pp 1129-1138.

[20]: Galerie A., Y. Wouters and M. Caillet, Materials Science Forum, Vols. 369-372 (2001), pp 231-238.

[21]: Holt A. and P. Kofstad, Solid State Ionics, Vol 69 (1994), pp 137-143.

[22]: Hultquist G., B. Tveten and E. Hörnlund, Oxidation of Metals, Vol. 54, N° 1/2 (2000), pp 1-10.

TABLE CAPTION

Table 1: Chemical compositions (mass %) of the model stainless steel alloys using ICP quantitative analysis. 16

Table 1: Chemical compositions (mass %) of the model stainless steel alloys using ICP quantitative analysis.

Nominal compositions	Fe	Cr	Ni	B	P	Si	C	S	N	O
Fe-10Cr	Bal.	9.44	<0.01	<0.001	0.002	0.02	0.0044	0.0044	0.0010	0.0608
Fe-12Cr	Bal.	11.85	<0.01	0.002	0.006	<0.01	0.0045	0.0045	0.0008	0.0548
Fe-14Cr	Bal.	13.84	<0.01	0.003	0.003	<0.01	0.0016	0.0052	0.0009	0.0609
Fe-16Cr	Bal.	15.71	<0.01	0.009	0.005	<0.01	0.0009	0.0046	0.0010	0.0657
Fe-18Cr	Bal.	17.78	<0.01	0.012	0.005	<0.01	0.0013	0.0043	0.0015	0.0554
Fe-20Cr	Bal.	19.64	<0.01	0.016	<0.002	<0.01	0.0017	0.0048	0.0008	0.0635
Fe-20Cr-30Ni	Bal.	19.59	30.07	<0.001	0.004	0.01	0.0020	0.0047	0.0044	0.0409
Fe-20Cr-25Ni	Bal.	19.52	24.82	0.007	0.004	<0.01	0.0018	0.0045	0.0024	0.0434
Fe-20Cr-20Ni	Bal.	19.68	20.12	<0.001	0.005	0.01	0.0010	0.0041	0.0009	0.0421
Fe-20Cr-15Ni	Bal.	19.38	15.27	0.002	<0.002	0.01	0.0020	0.0047	0.0008	0.0428
Fe-20Cr-10Ni	Bal.	19.85	9.89	0.002	<0.002	<0.01	0.0020	0.0050	0.0223	0.0944
Fe-18Cr-30Ni	Bal.	17.76	30.04	<0.001	0.004	<0.01	0.0010	0.0042	0.0006	0.0385
Fe-18Cr-25Ni	Bal.	17.53	24.60	0.006	0.008	<0.01	0.0017	0.0040	0.0006	0.0378
Fe-18Cr-20Ni	Bal.	17.75	20.05	0.003	0.004	0.01	0.0030	0.0036	0.0007	0.0464
Fe-18Cr-15Ni	Bal.	17.85	15.04	<0.001	0.004	0.01	0.0010	0.0042	0.0007	0.0564
Fe-18Cr-10Ni	Bal.	17.86	9.92	0.001	0.002	<0.01	0.0016	0.0046	0.0008	0.0441
Fe-16Cr-30Ni	Bal.	15.68	29.60	0.012	0.011	<0.01	0.0039	0.0031	0.0006	0.0356
Fe-16Cr-25Ni	Bal.	15.97	24.84	0.001	0.006	<0.01	0.0019	0.0040	0.0008	0.0373
Fe-16Cr-20Ni	Bal.	15.61	19.54	0.010	0.005	<0.01	0.0020	0.0038	0.0045	0.0351
Fe-16Cr-15Ni	Bal.	15.80	14.82	<0.001	0.004	<0.01	0.0019	0.0043	0.0009	0.0389
Fe-16Cr-10Ni	Bal.	15.79	9.88	<0.001	0.005	<0.01	0.0020	0.0045	0.0008	0.0494

FIGURE CAPTIONS

Figure 1: Light microscopy of etched Fe-Cr and Fe-Cr-Ni model samples after vacuum annealing at 1100°C and before oxidation. XRD results are indicated: A: Austenitic and F: Ferritic. 19

Figure 2: Effect of Ni content for Fe-16Cr-Ni (a), Fe-18Cr-Ni (b) and Fe-20Cr-Ni (c, with expanded Y axis scale) steels on specimen mass change for 1h cycles at 650°C in air plus 10% water vapor. POS: Protective Oxide Scale, AA: Accelerated Attack without spallation, AAS: Accelerated Attack with Spallation..... 20

Figure 3: Effect of Ni content for Fe-16Cr-Ni (a), Fe-18Cr-Ni (b) and Fe-20Cr-Ni (c) steels on specimen mass change for 1h cycles at 800°C in air plus 10% water vapor. POS: Protective Oxide Scale, AA: Accelerated Attack without spallation, AAS: Accelerated Attack with Spallation. 21

Figure 4: Effect of Cr content for Fe-Cr ferritic steels on specimen mass change for 1h cycles at 650°C (a) and 800°C (b and c with expanded Y axis scale) in air plus 10% water vapor..... 22

Figure 5: Light microscopy of the Fe-Cr-Ni sample surface after 100x1h cycles at 650°C under mixed air +10% water vapor. XRD results and SEM micrographs of the surface are shown..... 23

Figure 6: Light microscopy of the Fe-Cr-Ni sample surface after 100x1h cycles at 800°C under mixed air +10% water vapor. XRD results and SEM micrographs of the surface are shown..... 24

Figure 7: Light microscopy of the Fe-Cr sample surface after 100x1h cycles at 650 and 800°C under mixed air +10% water vapor. XRD results and SEM micrographs of the surface are shown..... 25

Figure 8: Light microscopy of polished sections of the oxide scales grown on Fe-Cr-Ni after 100x1h cycles at 650°C under mixed air +10% water vapor..... 26

Figure 9: Light microscopy of polished sections of the oxide scales grown on Fe-Cr-Ni after 100x1h cycles at 800°C under mixed air +10% water vapor. White block arrows in (b) and (c) indicate

oxide penetration at alloy grain boundaries. Gray block arrows in (a), (b) and (c) indicate microstructural defects such as pores or cracks. 27

Figure 10: Light microscopy of polished sections of the oxide scales grown on Fe-Cr-Ni after 100x1h cycles at 650 and 800°C under mixed air +10% water vapor. White block arrows in (a) indicate probable influence on grain orientation of scale growth..... 28

Figure 11: Maps of the 3 different behaviors (protective oxide scale (POS), accelerated attack without spallation (AA) and with spallation (AAS)) depending on Ni and Cr contents observed for 100x1h cycles under air+10% water vapor..... 29

Figure 12: Arrhenius plot of Cr coefficient diffusion in austenitic and ferritic alloys. Solid and dashed lines were calculated from Tökei et al. data [19] for bulk (a) and grain boundary diffusion with an average grain size of g = 150 µm (b), respectively..... 30

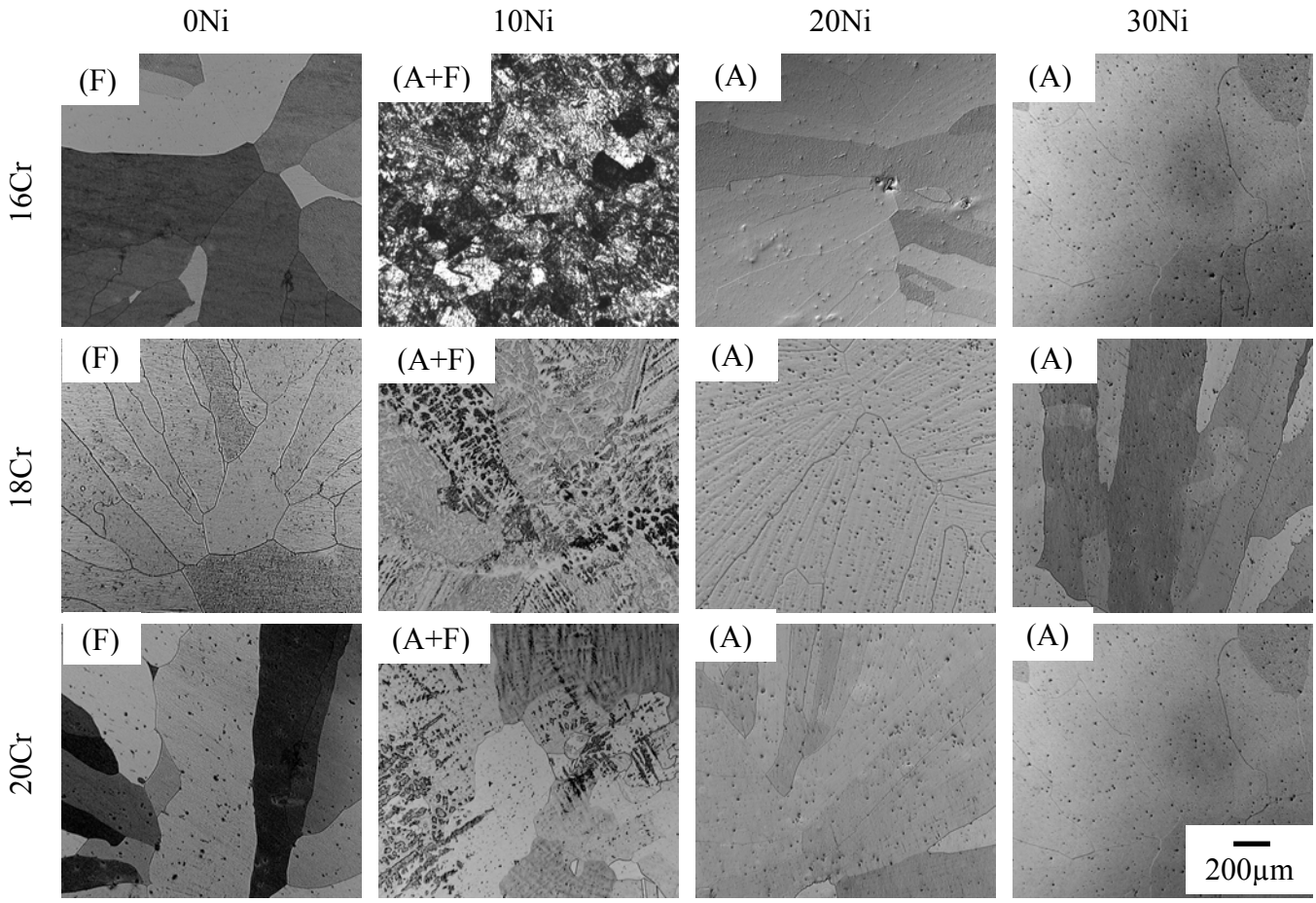

Figure 1: Light microscopy of etched Fe-Cr and Fe-Cr-Ni model samples after vacuum annealing at 1100°C and before oxidation. XRD results are indicated: A: Austenitic and F: Ferritic.

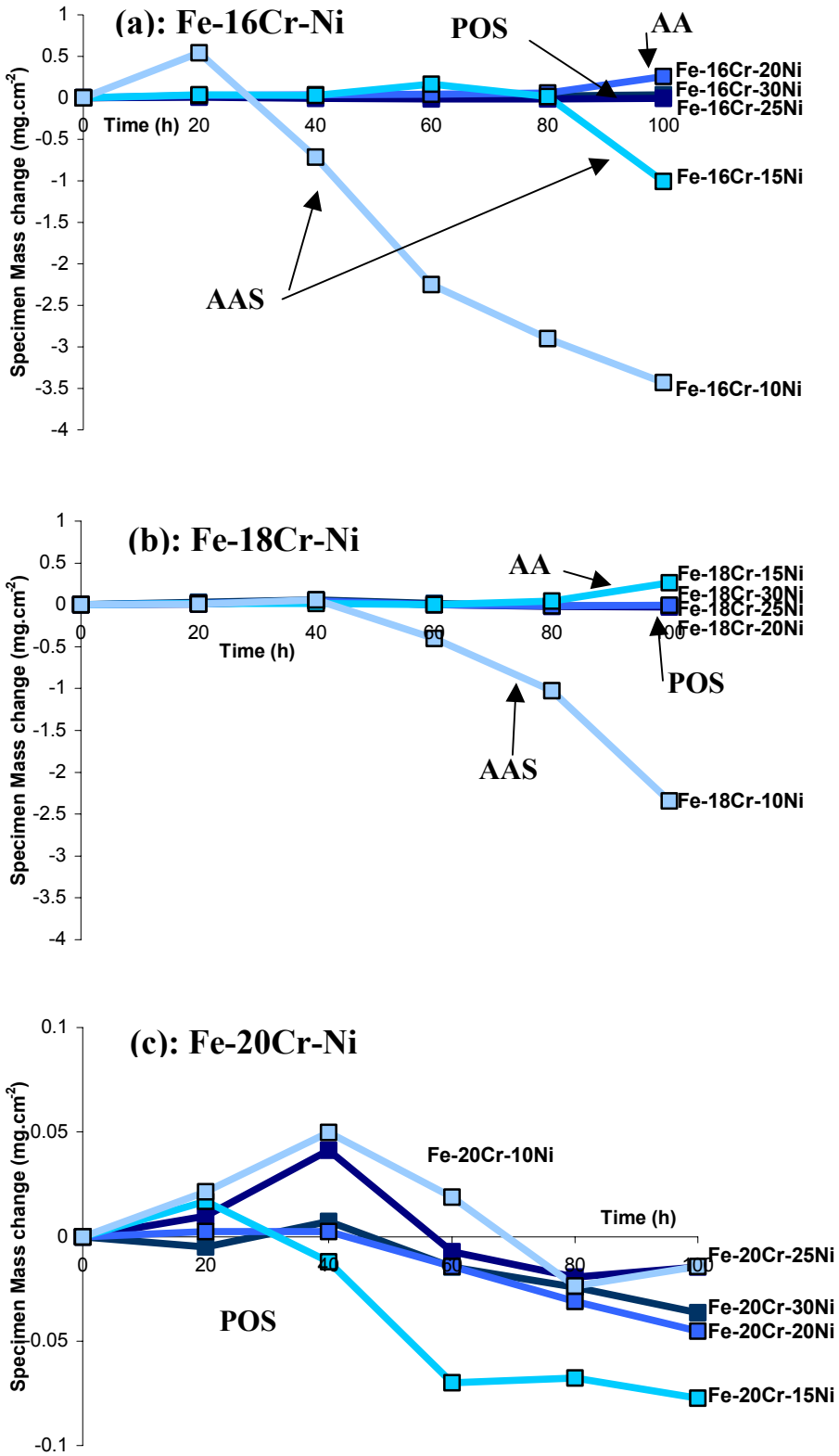

Figure 2: Effect of Ni content for Fe-16Cr-Ni (a), Fe-18Cr-Ni (b) and Fe-20Cr-Ni (c, with expanded Y axis scale) steels on specimen mass change for 1h cycles at 650°C in air plus 10% water vapor. POS: Protective Oxide Scale, AA: Accelerated Attack without spallation, AAS: Accelerated Attack with Spallation.

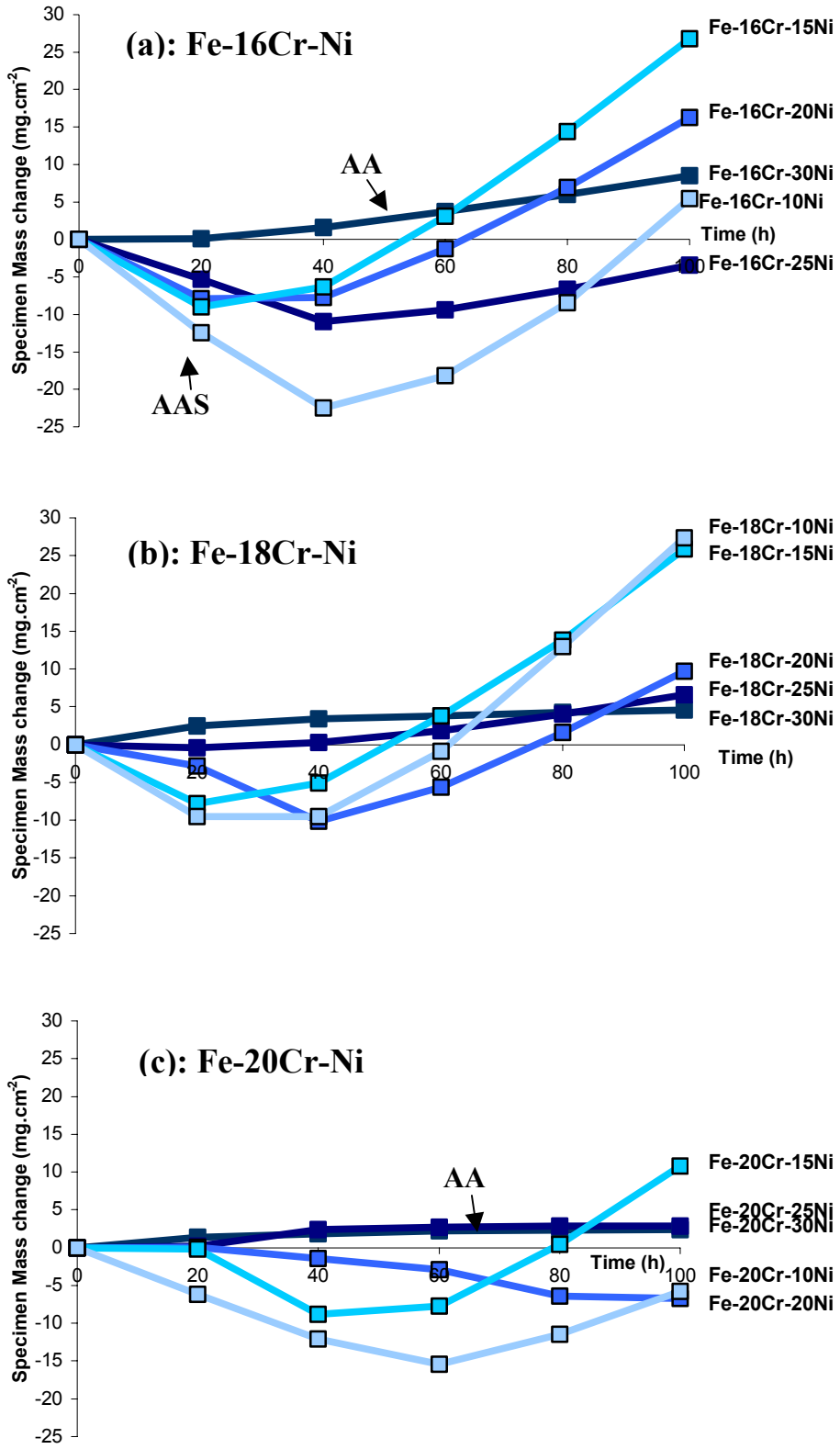

Figure 3: Effect of Ni content for Fe-16Cr-Ni (a), Fe-18Cr-Ni (b) and Fe-20Cr-Ni (c) steels on specimen mass change for 1h cycles at 800°C in air plus 10% water vapor. POS: Protective Oxide Scale, AA: Accelerated Attack without spallation, AAS: Accelerated Attack with Spallation.

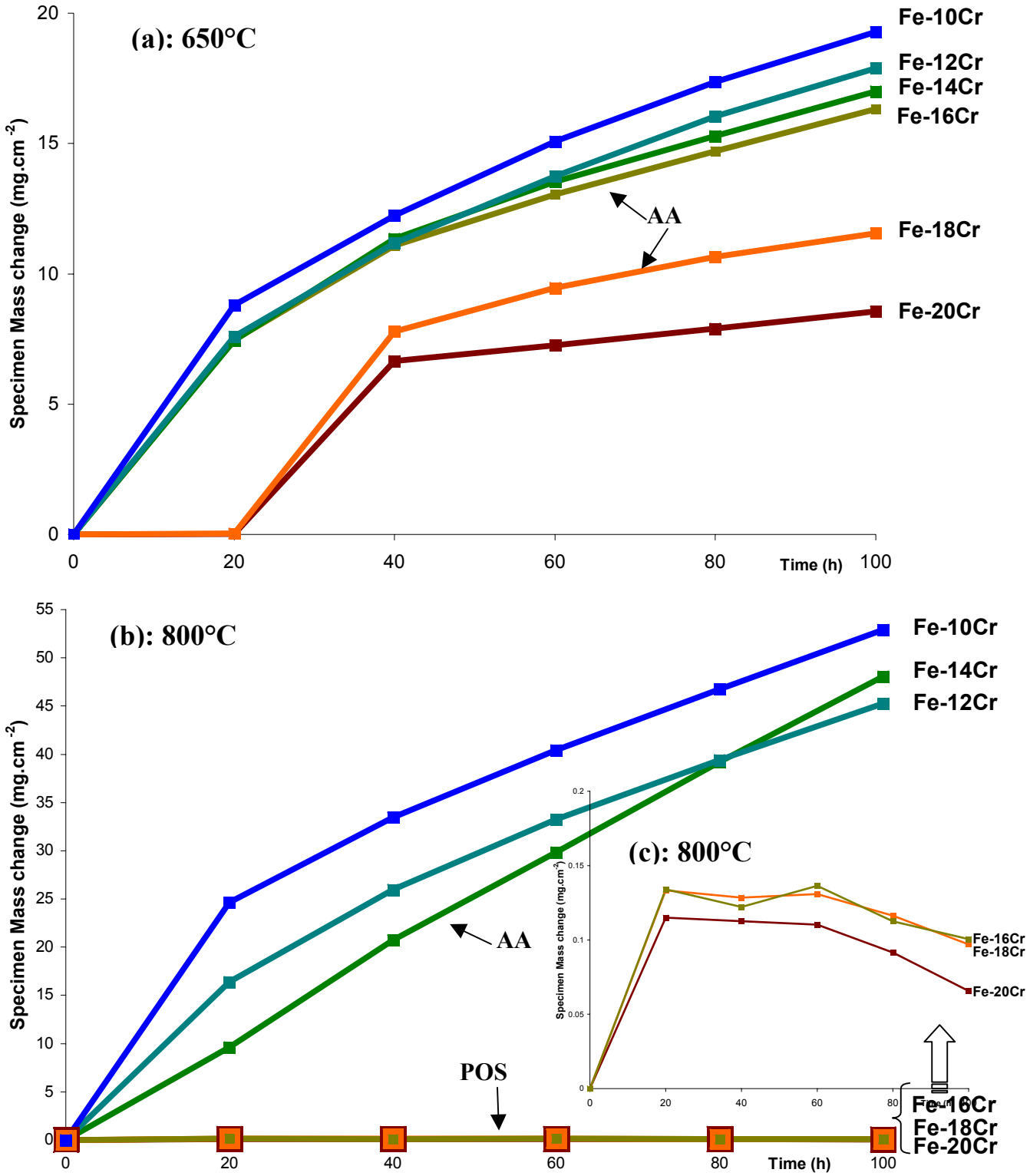

Figure 4: Effect of Cr content for Fe-Cr ferritic steels on specimen mass change for 1h cycles at 650°C (a) and 800°C (b and c with expanded Y axis scale) in air plus 10% water vapor.

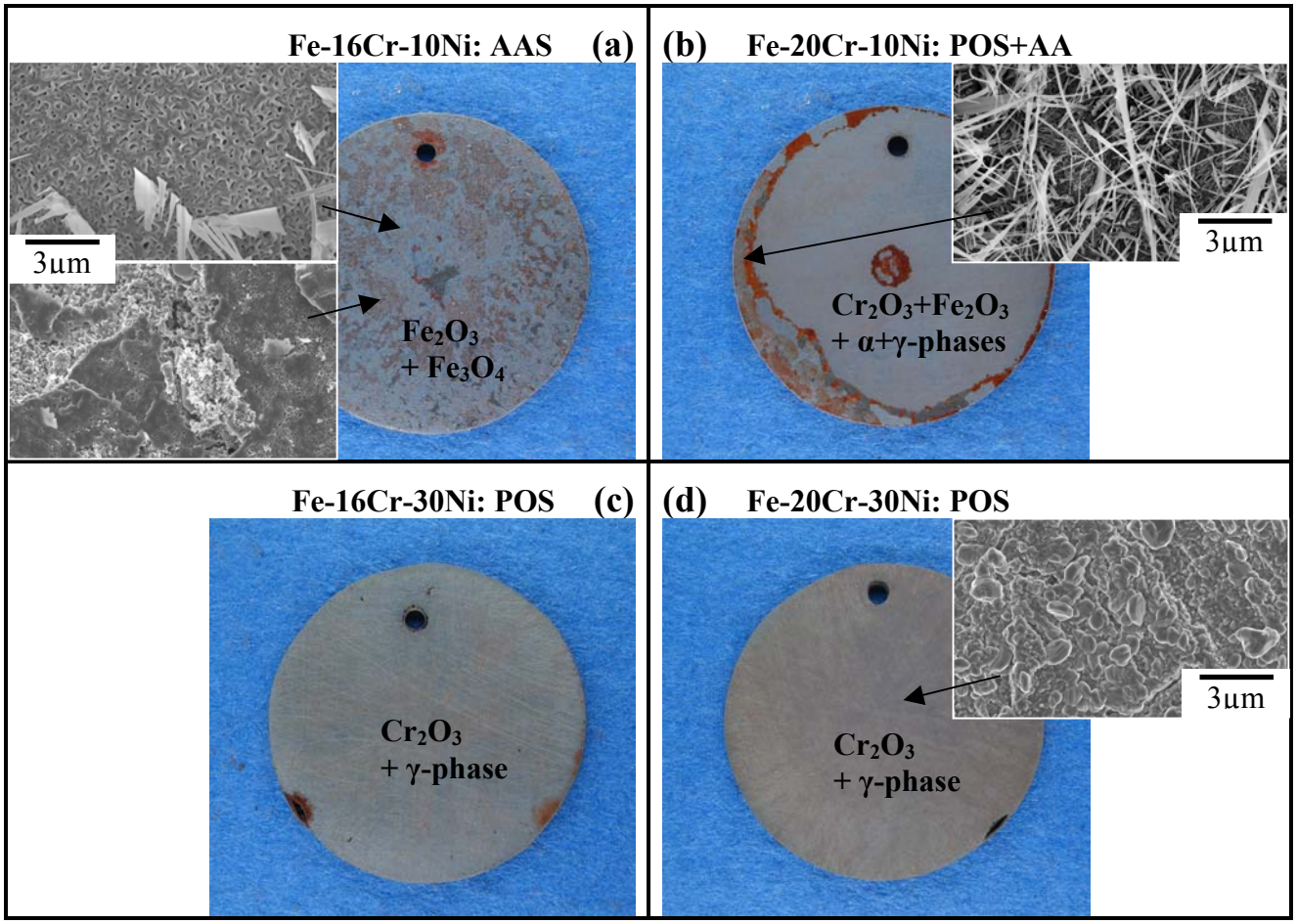

Figure 5: Light microscopy of the Fe-Cr-Ni sample surface after 100x1h cycles at 650°C under mixed air +10% water vapor. XRD results and SEM micrographs of the surface are shown.

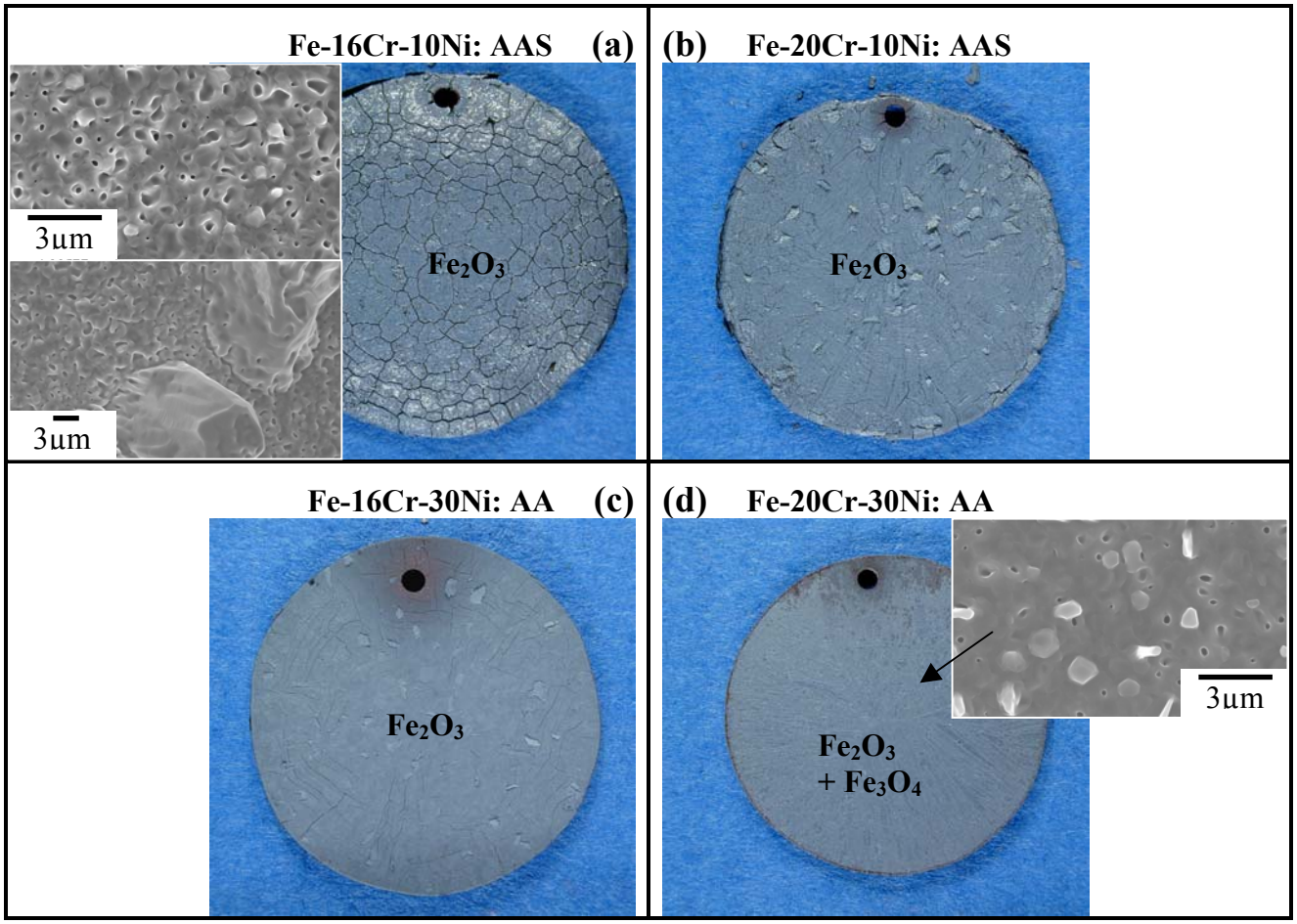

Figure 6: Light microscopy of the Fe-Cr-Ni sample surface after 100x1h cycles at 800°C under mixed air +10% water vapor. XRD results and SEM micrographs of the surface are shown.

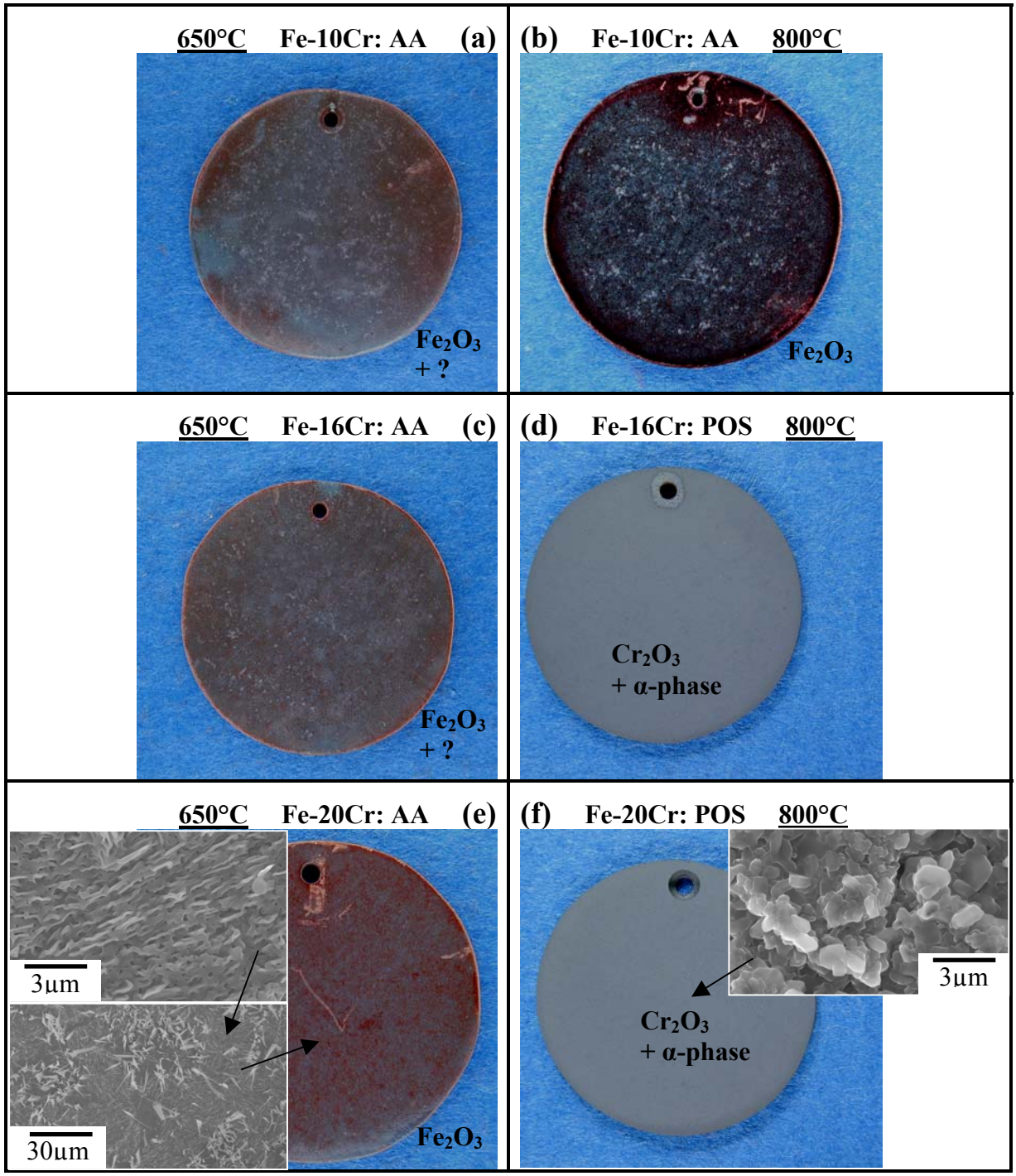

Figure 7: Light microscopy of the Fe-Cr sample surface after 100x1h cycles at 650 and 800°C under mixed air +10% water vapor. XRD results and SEM micrographs of the surface are shown.

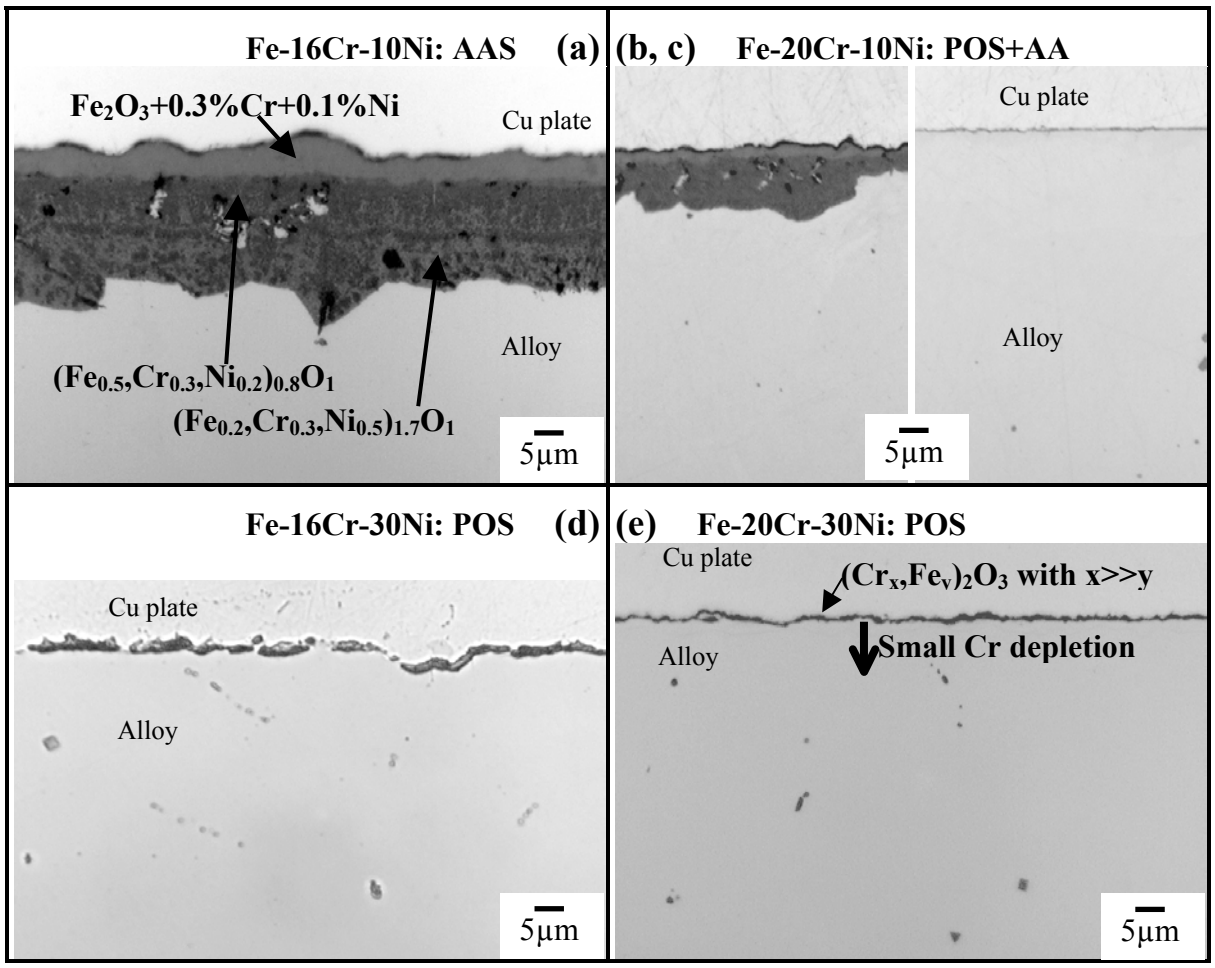

Figure 8: Light microscopy of polished sections of the oxide scales grown on Fe-Cr-Ni after 100x1h cycles at 650°C under mixed air +10% water vapor.

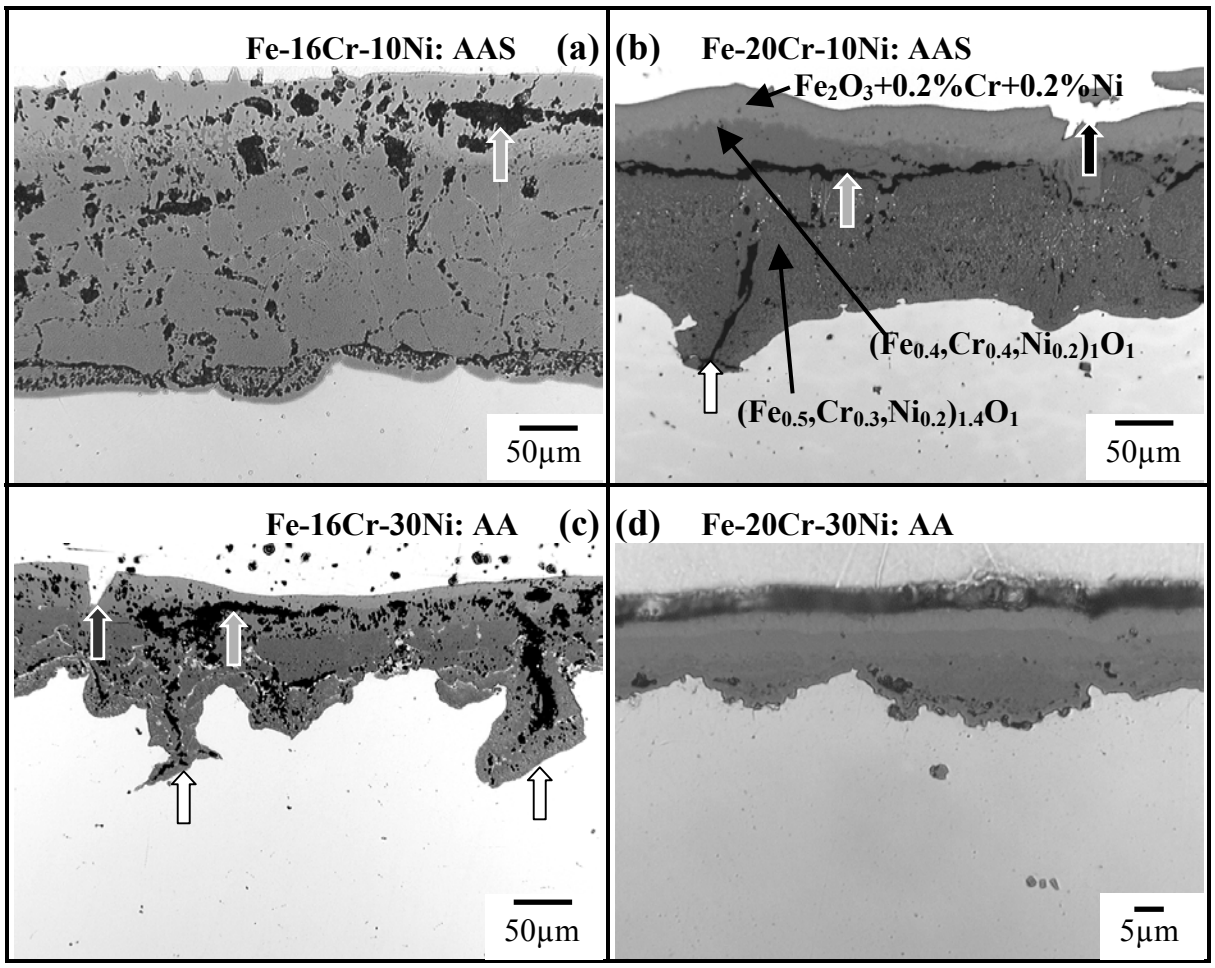

Figure 9: Light microscopy of polished sections of the oxide scales grown on Fe-Cr-Ni after 100x1h cycles at 800°C under mixed air +10% water vapor. White block arrows in (b) and (c) indicate oxide penetration at alloy grain boundaries. Gray block arrows in (a), (b) and (c) indicate microstructural defects such as pores or cracks.

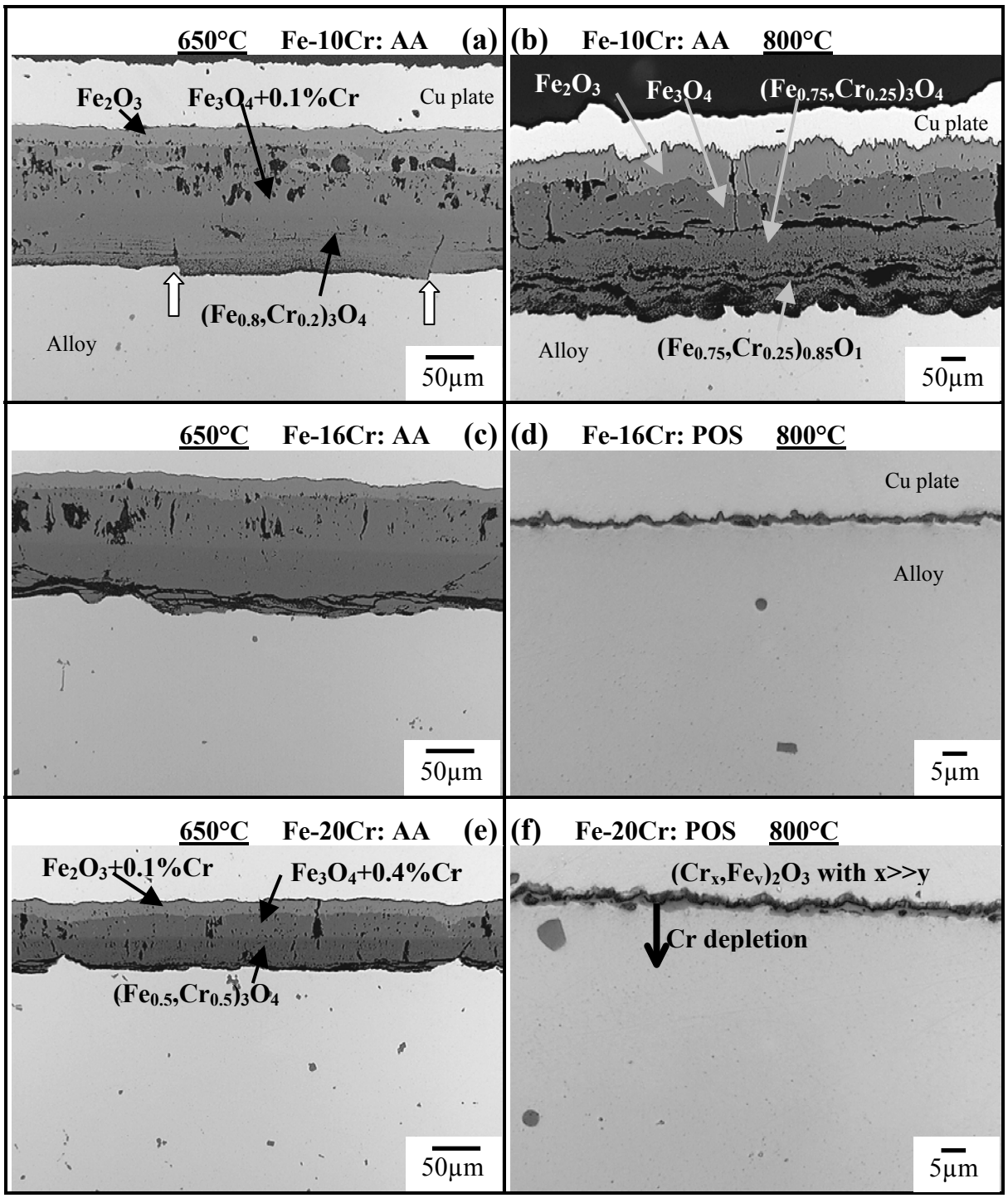

Figure 10: Light microscopy of polished sections of the oxide scales grown on Fe-Cr-Ni after 100x1h cycles at 650 and 800°C under mixed air +10% water vapor. White block arrows in (a) indicate probable influence on grain orientation of scale growth.

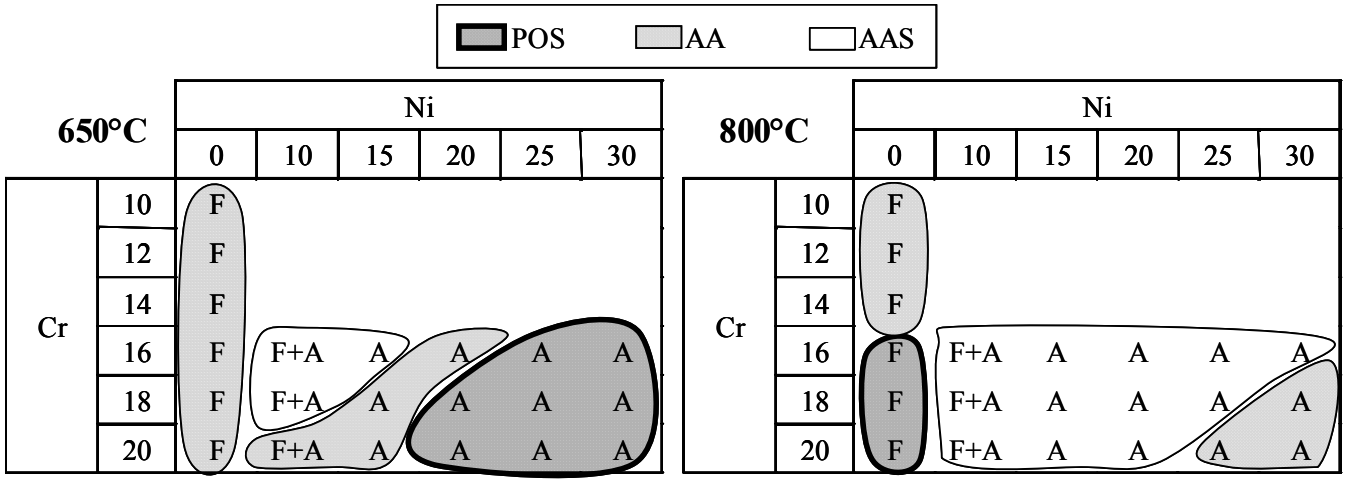

Figure 11: Maps of the 3 different behaviors (protective oxide scale (POS), accelerated attack without spallation (AA) and with spallation (AAS)) depending on Ni and Cr contents observed for 100x1h cycles under air+10% water vapor.

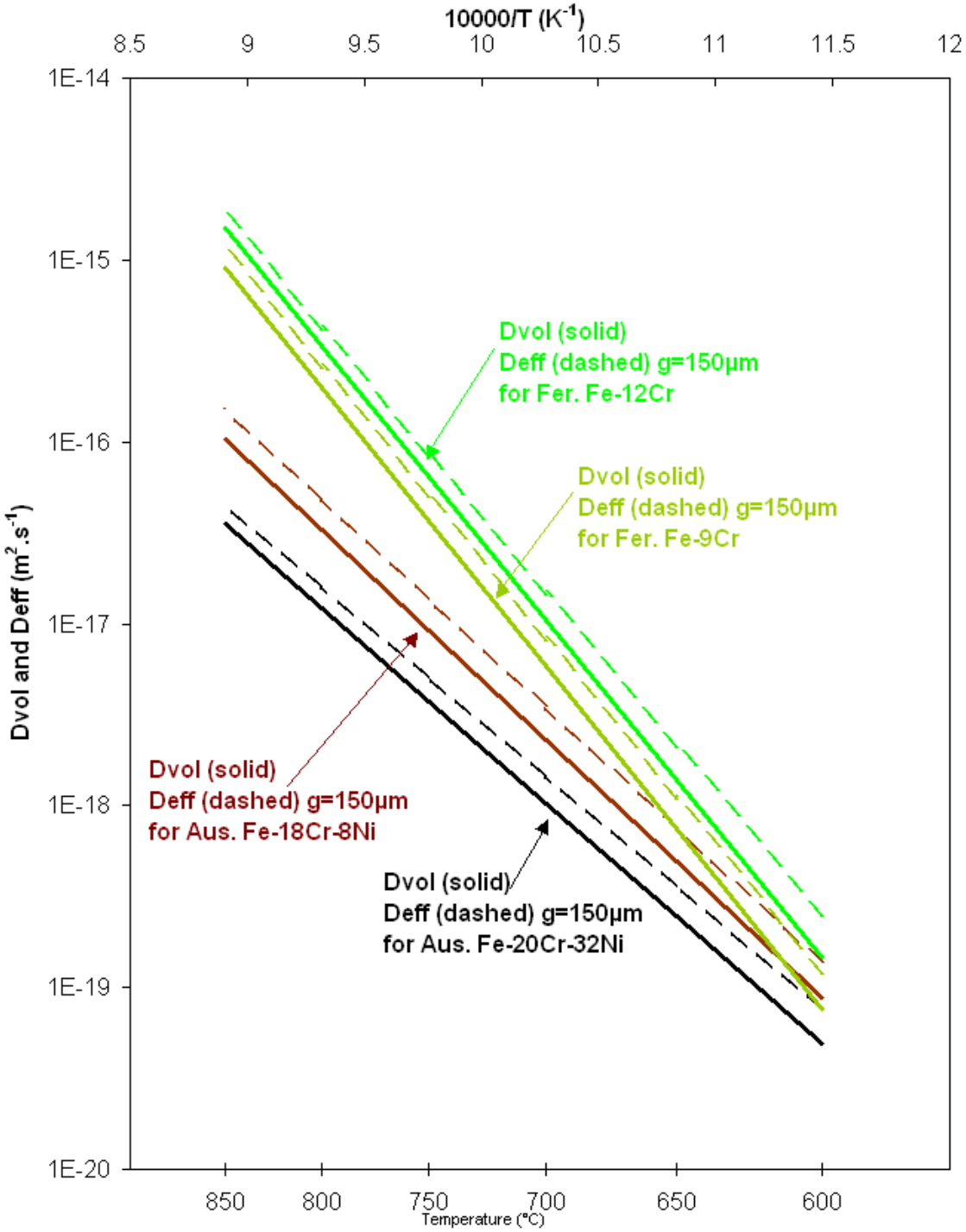

Figure 12: Arrhenius plot of Cr coefficient diffusion in austenitic and ferritic alloys. Solid and dashed lines were calculated from Tökei et al. data [19] for bulk (a) and grain boundary diffusion with an average grain size of g = 150 µm (b), respectively.